

Static Characteristics of Fire Hose Actuators and Design of a Compliant Pneumatic Rotary Drive for Robotics

Johannes T. Stoll¹, Kevin Schanz¹, Michael Derstroff¹ and Andreas Pott²

Abstract—In this work, we present and explain in detail the design of a new type of pneumatic actuator made of fire hose, the fire hose actuator (FHA), see Fig. 1. We model the force output of this type of actuator and we compare the theoretic results to the data measured on the laboratory test stand.

Furthermore, we present the design of a pneumatic rotary drive that is actuated by four of the above-mentioned FHAs. The drive unit features intrinsic compliance and it is capable of high-precision positioning. Due to these characteristics, the design concept of the rotary drive is suitable for the potential use in robotics, especially in human-robot collaboration. In addition, we model the static torque distribution of the rotary drive and we compare the theoretic results to the data measured on the realized laboratory test stand. Moreover, we discuss the most important characteristics of the rotary drive. Hence, we present measurements of the adjustable stiffness and we show that high-precision positioning is possible with the system, reaching in ideal areas every bit of the used 17-bit encoder with a resolution of 0.0027° . Moreover, the drive unit is capable of continuous rotation while the maximum continuous torque possible is found to be 63.1 Nm.

I. INTRODUCTION

A. Motivation

Today, in the field of safe and precise articulated robots, there are mainly three different approaches to realize their design. All three approaches use stiff and accurate robots as a starting point. Note that robots with soft structures are not considered in the following classification.

In the first approach, additional torque sensors in the joints detect unusual impacts. With this additional information, an advanced control system is realized that makes the robot behave compliant, see for example [1], [2].

In the second approach, the robot's structure is covered with a sensor skin. Depending on the type of sensor skin, the robot stops as soon as an object comes close to or actually touches the robot's skin, see for example [3–6].

The third approach to realize compliant articulated robots is to use drive units that are intrinsically compliant. Different compliant actuators can be used to realize compliant rotary drive units, see for example [7–10].

The main challenges for a rotary drive that comprises compliant actuators are to prove that the drive unit can

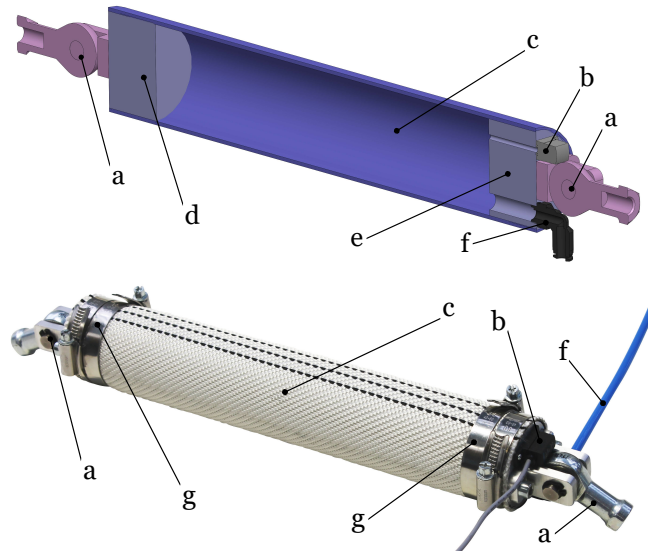


Fig. 1. Fire hose actuator (FHA), top: sectional of the 3D-CAD-model of the FHA, bottom: realized FHA, joint head for mechanical connection a, pressure sensor b, fire hose c, closed plug d, plug with pressure port and sensor port e, air pressure connection f, hose clamp g.

be controlled and positioned very precisely and that the delivered torque is sufficient for a robotic joint. If the above-mentioned characteristics are present, then an articulated robot that consists of several of these compliant rotary drives is capable of safe human-robot collaboration.

The rotary drives that we have investigated in previous works do not provide sufficient torque for the use in articulated robots. Hence, the motivation for the new pneumatic FHA and the rotary drive design that we present in this work is to prove that more than 50 Nm of continuous static torque can be delivered, while the key characteristics are again present. Thus, we show that the new rotary drive features intrinsic compliance, adjustable stiffness, continuous rotation and the capability to perform high-precision positioning. Moreover, we present a basic calculation of the force exerted by a FHA as well as measurements of the force. Based on these force measurements we create an improved force model of the FHA and we later on use it to derive the static torque distribution of the rotary drive. In addition to the theoretic description of the drive unit, we present measurements of the laboratory test stand and we compare theoretic and experimental data. Finally, we point out open questions and we give an outlook on how the design and the model of the FHA and the rotary drive could be improved in the future.

*This work was not supported by any organization.

¹Johannes T. Stoll, Kevin Schanz and Michael Derstroff are with the department 'Robot and assistive systems' at the Fraunhofer Institute for Manufacturing Engineering and Automation IPA, 70569 Stuttgart, Germany. johannes.stoll@ipa.fraunhofer.de

²Andreas Pott is with the Institute for Control Engineering of Machine Tools and Manufacturing Units (ISW), University of Stuttgart, 70174 Stuttgart, Germany. andreas.pott@isw.uni-stuttgart.de

B. Related Works

In other works, researchers have presented pneumatic actuators made of fire hose. In [11] and [12], the flexator pneumatic muscle rotary actuator has been presented. Two more designs that use fire hose to create pneumatic actuators are presented in [13]. In the coiled rotary elastic chamber (cREC) design, antagonistic coils of fire hose are used to realize a rotary drive, while the buckled rotary elastic chamber (bREC) design uses an antagonistic set of buckled fire hose working chambers to create a rotary drive. In [14], the rotary elastic chamber (REC) actuator is characterized, while in [15] the skewed rotary elastic chambers bending actuator (sRECBA) is presented. The sRECBA consist of three underlying skewed rotary elastic chamber-modules (sREC-modules) mounted on top of each other. All mentioned rotary drives are capable of operating in different angular ranges. However, none of these drive designs can operate more than 130° . The maximum static torque that these drive units deliver reaches up to 55 Nm for the bREC.

The mechanical design of the rotary drive that we present in this paper can be found in similar arrangements in the patents [16–18]. However, all mechanic designs described in the aforementioned patents are intended to be used as pneumatic motors that are designed to be operated at relatively high rpm while delivering a constant torque output on the drive shaft. These pneumatic motors are intended for a different use than the drive designs presented in the pending patent [19]. In this patent, we describe different configurations of drive units that avoid the stick-slip phenomenon by design. All designs presented are intended to serve as robotic joints, operating at slow speeds, delivering a variable torque and with the possibility to perform high-precision positioning. Hence, even if similarities in the design of the above-mentioned drive units can be found, the characteristics as well as the control system and the potential application of the drive units are significantly different.

As mentioned above, we have investigated different drive units and different types of pneumatic working chamber in previous works, see [8], [9]. All drive units use actuators with variable volume and flexible walls. As a result, we could avoid the well-known stick-slip phenomenon, described for example in [20], [21] in all the investigated rotary drives. This is very important as it often prevents high-precision positioning of pneumatic drive units. Moreover, in [22] we present the mechatronic control system that we use to control the rotary drive, which we presented in [9], in detail. We use this control system also throughout the present work.

II. MECHANICAL DESIGN

A. Design of the Fire Hose Actuators

We present a simple yet new type of pneumatic actuator, the fire hose actuator. In Fig. 1, a sectional of the 3D-CAD-model and the finally realized FHA, including all directly connected elements, are depicted. This type of actuator consist of a fire hose that is cut to the desired length and the open ends are closed with aluminum lids. We use two hose clamps

with the locks mounted opposed to each other to install the lids airtight at the ends of the fire hose section. Both aluminum lids allow the mechanic connection of joint heads, one of them additionally enables the pneumatic connection and the connection of a pressure sensor. The joint heads on the one hand hold the working chamber in place, but on the other hand allow the necessary flexibility, that the working chambers need, to be used later on in a drive unit. The FHA has to be flattened or compressed by an object to exert a force. When air pressure is applied to the deformed FHA, it tries to restore its original circular cross-sectional area. As a result, the FHA exerts a force onto any object that previously deformed its ideal shape. Details of the mechanical specifications of the FHA presented in this work can be found in the Appendix in Table I.

B. Design and Operating Principle of the Rotary Drive

A new rotary drive, depicted in Fig. 2, is designed that makes use of the FHAs presented above. The principal idea is to use the FHAs to exert a pushing force onto an eccentric roller element that is pivoted around the drive shaft.

In the well-known piston engine, a similar configuration can be found. In that case, the pistons are linked to the crankshaft via connecting rods and they exert pushing forces that cause the drive shaft to rotate. In the presented rotary drive, the FHAs exert a pushing force onto the roller element and this leads, due to the eccentricity of the roller, to a torque on the drive shaft and hence causes the drive shaft to rotate. Thus, the torque $M_{fha,i}$ generated by one of the FHAs varies in direction and quantity over the possible 360° of continuous rotation. Moreover, the eccentric roller element is pivoted around the drive shaft to avoid tangential forces between the FHAs and the eccentric roller. A sectional of the 3D-CAD-model as well as the realized rotary drive are depicted in Fig. 2. In the sectional, the fixed structure of the drive unit is tinted brown. The structure consists of a horizontal base plate on which the end plates that hold the shaft bearings are mounted. Moreover, the counterparts that hold the reacting forces of the FHAs are installed in two frame parts that are also mounted on the base plate and tinted brown. The shaft bearings as well as the bearings that pivot the eccentric roller are tinted red. The drive shaft is tinted in light green, while the eccentric roller is tinted in dark green. We use a 17-bit absolute encoder to measure the position of the drive shaft, tinted yellow. The FHAs and the connecting joint heads are tinted in the same colors as in Fig. 1, blue and pink. All relevant mechanical parameters of the rotary drive, are listed in Table I. A simple explanation of the operating principle can be found in the animation part of the video accompanying this paper.

The design of the FHA as well as the drive design presented in this work are both representing a proof of concept and are designed with a focus on stability and durability to enable precise measurement and thorough testing. As a result, the rotary drive is relatively bulky and heavy and cannot be right away implemented in a robotic system.

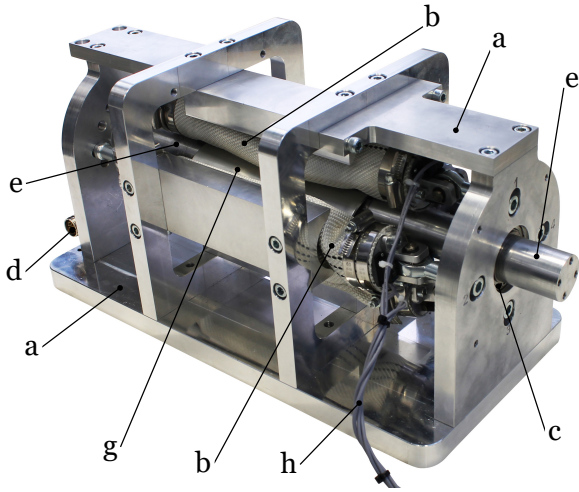
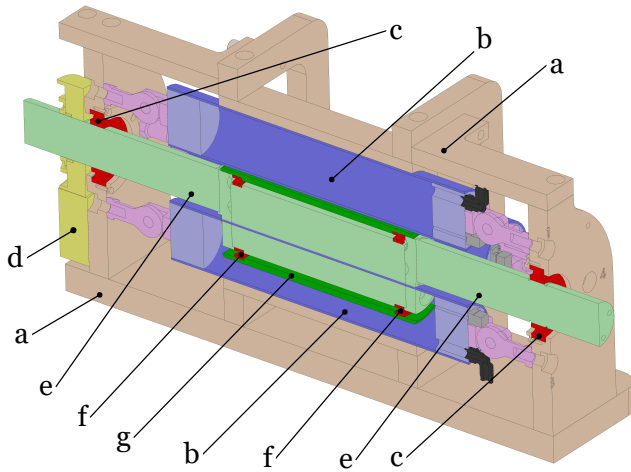


Fig. 2. Rotary drive unit, top: sectional of the 3D-CAD-model, bottom: realized rotary drive unit, structure a, FHA b, shaft bearing c, absolute encoder d, drive shaft e, roller bearing f, eccentric roller g, connecting cable of pressure sensors h.

C. Laboratory Test Stand

In Fig. 3, an overview of the realized laboratory test stand is depicted. We use $n = 4$ FHAs in the modular laboratory test stand throughout this work. The control system consists of a programmable logic controller (PLC) and one associated proportional valve per FHA. The pneumatic setup and the mechatronic control system are described in detail in [22] and therefore not presented in this work.

III. MODELLING

In this section, we present a basic model of the static force exerted by the FHAs onto a roller element and we derive the equations that describe the static torque distribution of the rotary drive.

A. Static Force of the FHA

The FHAs exert a pushing force onto the eccentric roller, when pressure is applied. The force F_{fha} exerted by a FHA can be described as the effective surface A_{eff} multiplied with

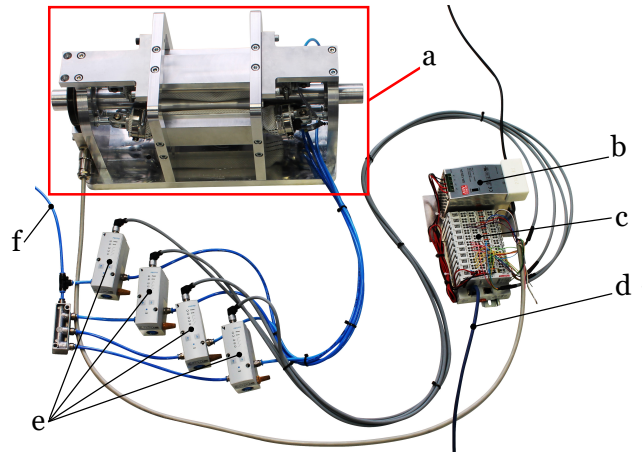


Fig. 3. Overview of the laboratory test stand, drive unit a, power supply b, PLC control c, Ethernet connection d, proportional valves e, air supply f.

the applied pressure level p_{fha}

$$F_{fha} = p_{fha}A_{eff}. \quad (1)$$

The pressure level is known, since it is set by the proportional valves. Moreover, it can be measured with the pressure sensor mounted on one of the lids of the FHA. The effective surface cannot be easily determined, therefore, it has to be approximated. A basic approach for this approximation is to calculate the effective width w_{eff} of the section line of the FHA and the intersecting element normal to the longitudinal axis of the FHA and to multiply this distance with the active length of the FHA. The active length of the FHA, l_{fha} is a design parameter and equal to the length of the roller element and to the length of the support structure and thus constant. Hence, it follows

$$A_{eff} = w_{eff}l_{fha}. \quad (2)$$

We modified the laboratory test stand to characterize the actuators by measuring the static force exerted by the FHA onto the eccentric roller when both parts are aligned vertically. In Fig. 4, a schematic representation of a sectional of the laboratory test stand in the vertically aligned force measurement configuration is depicted. The origin of the coordinate system $P1$ is referenced to the structure of the test stand and therefore fixed. It can be seen that the vector $\overrightarrow{P1P2}$ is colinear to $\overrightarrow{P2P3}$ and to d and orthogonal to the section line of the roller and the FHA $\overrightarrow{P4P5}$.

To characterize the static force, we varied the position of $P2$ along the y-axis. This change in the position of $P2$ implies a change of the section line of the roller and the ideal FHA, $\overrightarrow{P4P5}$. We assume that the effective width w_{eff} of the FHA corresponds to the length $|\overrightarrow{P4P5}|$, as can be seen in Fig. 4. We verified this assumption by integrating the distributed load, which results from the pressure inside the FHA, from $P4$ to $P5$ along $\overrightarrow{P4P5}$ and along the outer surface of the green roller in Figure 4. Both calculations yield the same resulting force vector. As a result, the force exerted from a FHA onto the roller finally depends on the distance $|\overrightarrow{P2P3}|$ and on the

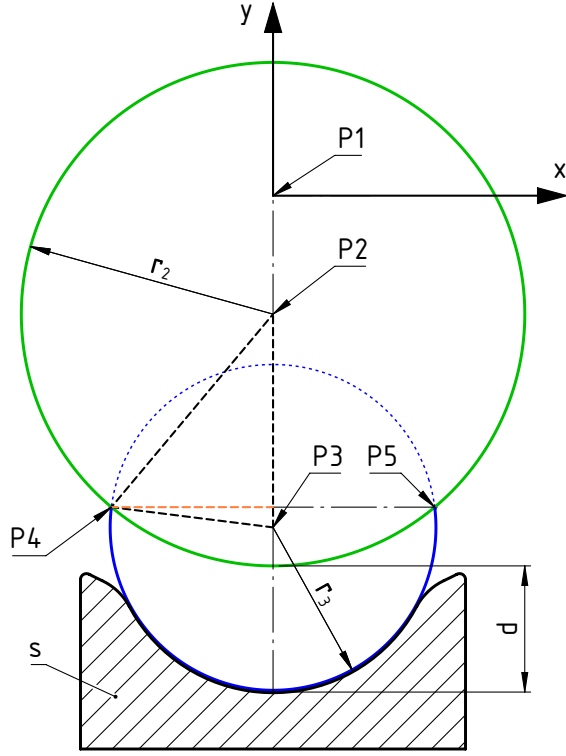


Fig. 4. Schematic of the force modelling and measurement, sectional of the laboratory test stand in the force measurement configuration, the sectional is perpendicular to the longitudinal axis of the FHA, support structure of the FHA s , origin of the coordinate system $P1$, roller element green, center of the roller element $P2$, radius of the roller element r_2 , ideal FHA blue, center of the FHA $P3$, radius of the FHA r_3 , intersection points of the ideal FHA and the roller element $P4$ and $P5$, distance between roller and structure d , altitude of the triangle $P2, P3, P4$ dashed orange line.

pressure level applied to the FHA. Therefore, we derive the basic force model to

$$F_{fha} = f(p_{fha}, |\overrightarrow{P2P3}|) = p_{fha} l_{fha} |\overrightarrow{P4P5}|. \quad (3)$$

The material of the used fire hose is elastic and, thus, the radius r_3 of the FHA is slightly increasing with increasing pressure. The support structure of the FHA is fixed and the FHA linked with joint heads to the structure. Hence, point $P3$ slightly changes its position due to a variation of the radius r_3 depending on the inflating pressure p_{fha} . The described change of the radius r_3 is measured with a caliper and approximated linearly to

$$r_3(p_{fha}) = 0.5 \cdot 10^{-9} \cdot p_{fha} + 28.7 \cdot 10^{-3}. \quad (4)$$

As a result, the length $|\overrightarrow{P2P3}|$ depends on both, the position of $P2$ and on the position of $P3$ and thus on the pressure level applied to the FHA. The distance $|\overrightarrow{P4P5}|$ is found to be twice the altitude of the triangle $P2, P3, P4$, depicted in Fig. 4 as the dashed orange line. Since $|\overrightarrow{P2P4}| = r_2$, $|\overrightarrow{P3P4}| = r_3$ and with $|\overrightarrow{P2P3}|$ set as a geometric parameter, all distances in this triangle are known. Hence, the double altitude in terms of the sides and therefore $|\overrightarrow{P4P5}|$ can

be calculated as

$$|\overrightarrow{P4P5}| = 2 \cdot \frac{2\sqrt{\sigma(\sigma - |\overrightarrow{P2P3}|)(\sigma - r_2)(\sigma - r_3)}}{|\overrightarrow{P2P3}|} \quad (5)$$

with

$$\sigma = \frac{|\overrightarrow{P2P3}| + r_2 + r_3}{2}. \quad (6)$$

To improve the basic model, we map the measured force in Subsection IV-A to the applied pressure, p_{fha} , and the current distance, d , which is only depending on the position of $P2$. This leads to the relation

$$F_{fha} = f(p_{fha}, d). \quad (7)$$

B. Static Torque Distribution of the Rotary Drive

Based on the presented calculation of the force of a single FHA, we now derive a mathematical model that describes the static torque distribution of the rotary drive. A schematic representation of the parameters that we use to model the torque is depicted in Fig. 5, where only one FHA is depicted for better visibility. It is clear that the overall torque on the drive shaft is a result of all the torques generated by all FHAs, and therefore

$$M_{total}(\varphi) = \sum_{i=1}^n M_{fha,i}(\varphi_i) = \sum_{i=1}^n F_{fha,i}(p_{fha}, \varphi_i) l_{eff,i}(\varphi_i). \quad (8)$$

We rotate the position to each FHA i with $n = 4$ via

$$\varphi_i = \varphi - \frac{i-1}{n} 2\pi, \quad (9)$$

to describe the static torque with one single formula for every FHA. The torque generated by one FHA is a result of its force $F_{fha,i}$, which was derived in section III-A, multiplied with the effective lever arm $l_{eff,i}$. The effective area A_{eff} still depends on the chamber length of the FHA l_{fha} and $w_{eff}(\varphi_i)$, but the latter is now a function of the angular position φ_i , which leads to

$$A_{eff} = l_{fha} w_{eff}(\varphi_i). \quad (10)$$

The effective width w_{eff} represents the distance between the two intersection points of the eccentric roller and the fully inflated and round FHA, marked as $P4$ and $P5$ in Fig. 5. The aforementioned dependency on φ results from the fact that the angular position directly affects the position of $P2$ and thus, via the triangle Equation (5), the distance $|\overrightarrow{P4P5}|$. The center point of the eccentric roller, $P2$, rotates around the origin of the coordinate system, whereas $P3$, the center of the FHA, remains on the y -axis. Therefore, the positions of $P2$ and $P3$ are

$$P2 = \begin{pmatrix} -r_1 \sin(\varphi_i) \\ r_1 \cos(\varphi_i) \end{pmatrix}, \quad P3 = \begin{pmatrix} 0 \\ P7_y + r_3(p_{fha}) \end{pmatrix}. \quad (11)$$

Used in Equation (5) for $|\overrightarrow{P2P3}|$ and inserted in Equation (3), this leads to the force $F_{fha,i}$.

The effective lever arm is depicted in Fig. 5 as orange dashed line connecting the points $P1$ and $P6$, $l_{eff} = |\overrightarrow{P1P6}|$.

IV. RESULTS

A. Static Force of the Fire Hose Actuators

We use the force measurement configuration depicted in Fig. 4 to characterize the presented fire hose actuators. In this configuration the eccentricity is set to zero. Hence, the center of the roller is always positioned on the y-axis straight above the FHA. The roller itself is now pivoted on the one end and a force sensor prevents a motion of the roller on the opposite end. We use precise washers to increase the distance d between the roller and the support structure of the FHA in steps of 4 mm. Thus, we measure the exerted force for 11 different positions of $P2$ and for pressure levels from 100 kPa to 600 kPa with an increase of 100 kPa per measurement series. As a result, we present the measured relation stated in Equation (7) between the applied pressure p_{fha} , the distance d and the output force F_{fha} . The FHA exerts a maximum force of 8089 N at 600 kPa and $d = 18$ mm. The results are depicted in Fig. 6.

In Fig. 7, we compare the basic force model that we stated in Equation (3) to the data measured on the laboratory test stand. For the sake of clarity, the comparison in Fig. 7 only depicts the data sets for 200 kPa, 400 kPa and 600 kPa.

The theoretic force model of the FHA does not match well with the data obtained in measurements of the real FHA. Hence, as stated in Equation (7), we present an approximation of the relation that maps the force F_{fha} exerted by an FHA to the pressure p_{fha} and to the distance d . We expect that the reason for the mismatch of the basic model and the measurement data is that the real FHA is not circular as assumed in the model. Instead, the FHAs' circumferential length is constant or almost constant and its shape is significantly deformed by the roller. In the model, we do not account for this deformation, thus modelling the deformation could lead to an improved model of the effective width, w_{eff} .

Instead of improving the basic force model, we analysed the measurements to obtain a mathematical approximation of the FHA. A linear relation between applied pressure and exerted force for any given distance can be observed in Fig. 6. Thus, we use the linear model

$$F_{fha} = 2 \cdot (m(d) \cdot p_{fha} + c(d)), \quad (14)$$

in which the gradient m and the offset c are dependent on d , to approximate the force of the FHA. The gradient and the offset have to be derived separately. We approximate both by polynomials, in case of the gradient by the second order polynomial

$$m(d) = -2.34557d^2 + 0.0228089d + 0.00698647 \quad (15)$$

and in case of the offset by the third order polynomial

$$c(d) = -1207690d^3 + 223075d^2 - 14006.8d + 263.43. \quad (16)$$

Both equations show an error margin of less than one percent compared to the measured data. We use this more accurate description of the force to replace the force in Equation (3) and obtain better results for the simulation of the static torque

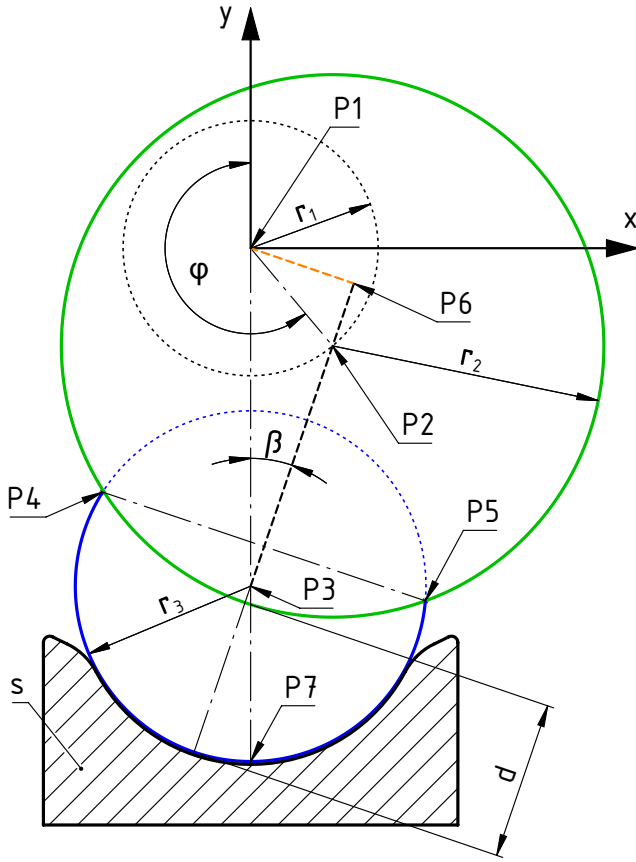


Fig. 5. Schematic of the torque modelling and measurement, laboratory test stand in the rotary configuration, sectional of the drive unit perpendicular to the longitudinal axis of the FHA and the drive shaft, only one FHA is depicted, current angular position φ , support structure of the FHA s , axis of rotation of the drive shaft and origin of the coordinate system $P1$, eccentric roller element green, center of the roller $P2$, radius of the roller r_2 , ideal FHA blue, center of the FHA $P3$, radius of the FHA r_3 , intersection points of the ideal FHA and the roller element $P4$ and $P5$, distance between roller and structure d , the line connecting $P2$, $P3$ and $P6$ is depicted as dashed black line, the line connecting $P1$ and $P6$ is perpendicular to the dashed black line and depicted as dashed orange line, intersection point of y-axis with the support of the FHA $P7$.

We apply the cosine theorem in the triangle $P1$, $P2$, $P3$ to calculate the angle β ,

$$\beta = \cos^{-1} \left(\frac{|\overrightarrow{P1P3}|^2 + |\overrightarrow{P2P3}|^2 - r_1^2}{2|\overrightarrow{P2P3}||\overrightarrow{P1P3}|} \right), \quad (12)$$

and with the sine function the effective lever arm is derived to

$$|\overrightarrow{P1P6}| = \begin{cases} -|\overrightarrow{P1P3}| \sin(\beta) & \text{for } 0 \leq \varphi_i < \pi \\ |\overrightarrow{P1P3}| \sin(\beta) & \text{for } \pi \leq \varphi_i < 2\pi \end{cases}. \quad (13)$$

The FHAs exert the forces $F_{fha,i}$ unto the eccentric roller. Multiplying these forces with the effective lever arms $l_{eff,i}$ leads to the total torque on the drive shaft, as stated in Equation (8). This, together with the approximation of the force stated in Equation (14), results in the model of the torque over 360° as depicted in the dashed lines in Fig. 9.

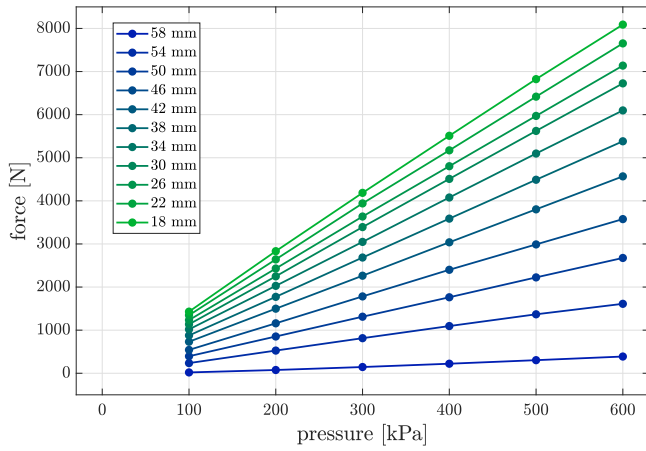


Fig. 6. Characterization of the FHA, relation between the exerted force F_{fha} and the pressure p_{fha} for different distances d between the roller element and the structure.

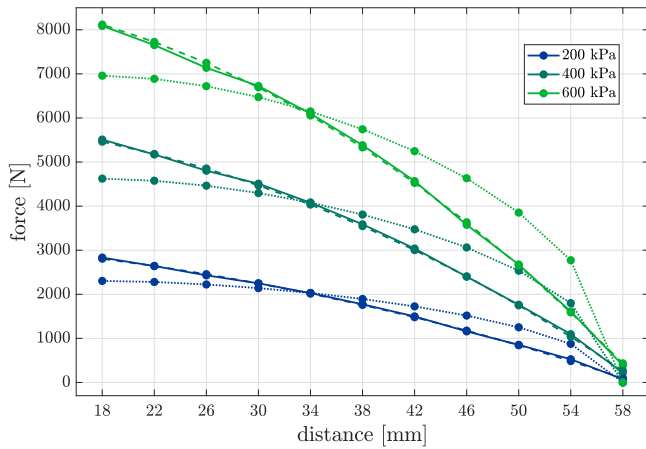


Fig. 7. Comparison of the basic force model, the measured force and the approximation of the measured force of the FHA. The graphs display the mappings from distance d to the output force of the FHA at different pressure levels. The measured values are displayed as solid lines, the mapping derived from the measured values as dashed lines and the basic mathematical model as dotted lines. For better legibility the legend only displays the color scheme for the measured values.

distribution. This approximation of the force is depicted as dashed lines in Fig. 7.

B. Static Torque Distribution of the Rotary Drive

In Fig. 8, the measured static torque distribution at various pressure levels is depicted. We measure the static torque on the drive shaft using a lever arm and a force sensor. This force, and therefore the torque, is measured in incremental steps of 15° . We observe that the FHA tends to move out of its intended position in certain situations. Basically, the FHA squeezes out of its longitudinal position towards the side with more space, therefore, we call this the squeeze-out effect. In Fig. 5, for example, the FHA would try to squeeze-out towards the gap between $P4$ and the structure on the left side. This effect is especially present at higher pressure levels and in the position in which d is minimal. Hence, we observe the squeeze-out effect in the schematic

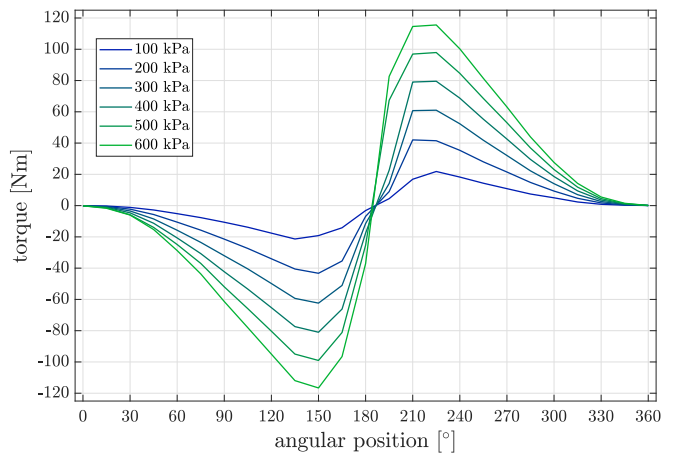


Fig. 8. Static torque distribution effected by FHA 1 at pressure levels from 100 kPa to 600 kPa.

representation in Fig. 5 for φ_i from 90° to 180° , while we do not notice the effect for all other values of φ_i . Moreover, we observed that the squeeze-out effect depends on the direction of rotation of the drive shaft and the roller. In cases where the roller rotates into the FHA, it is pushing the FHA out of its position and the squeeze-out is higher. When the roller is moving away from the FHA, and the FHA pushes the roller, the squeeze-out is lower. In Fig. 8, the zero crossing is expected to happen exactly at 180° , but an offset of a few degrees can be observed. We assume that this zero crossing offset is caused by the squeeze-out effect of the FHA.

The composition of the measured and of the calculated total static torque at a pressure level of 600 kPa is depicted in Fig. 9. The total static torque is the sum of all single torques acting in the same direction and it is likewise depicted for the model and the measurements. The maximum possible continuous static torque based on the measurements is found to be 63.11 Nm. As mentioned above, a difference between the theoretical and the measured zero crossing can be observed. Furthermore, this difference varies for the different FHAs. See for example the zero crossing difference of FHA 2 around 270° versus the zero crossing difference of FHA 4 around 90° . We assume that it is caused by the squeeze-out effect.

C. Adjustable Stiffness

In Fig. 10, we present measurements of the adjustable stiffness. A constant pressure level is applied to FHA 1 and FHA 3. The measurement starts at the position resulting from the applied pressure level. The proportional valves keep the pressure in the FHA constant during the experiment. We apply an external torque on the drive shaft and measure its deflection. The obtained data set shows quite linear characteristics and proves that adjustable stiffness can be realized with this system.

D. Position Control of the Rotary Drive

As stated in Subsection I-B, we avoid the stick-slip phenomenon and are therefore able to realize precise positioning

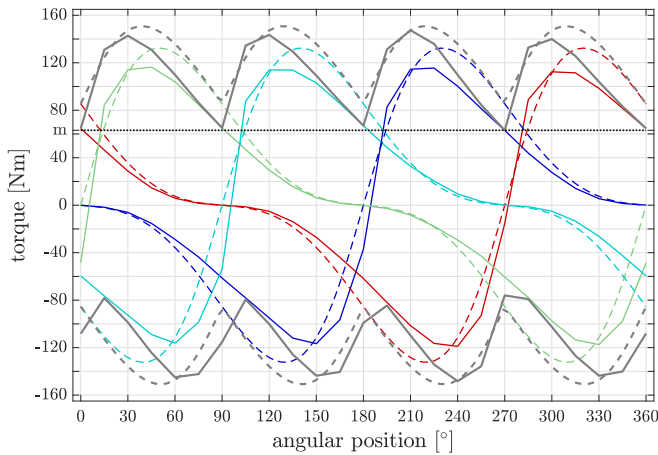


Fig. 9. Measured and calculated values of the static torque distribution for the configuration with $p=600$ kPa. Measured values are represented by continuous lines, calculated values are represented by dashed lines. The static torque distribution for each PAM is colored: blue for FHA 1, red for FHA 2, green for FHA 3, turquoise for FHA 4. The total static torque distribution is depicted grey and the dotted line at 63.11 Nm depicts the maximum possible continuous torque.

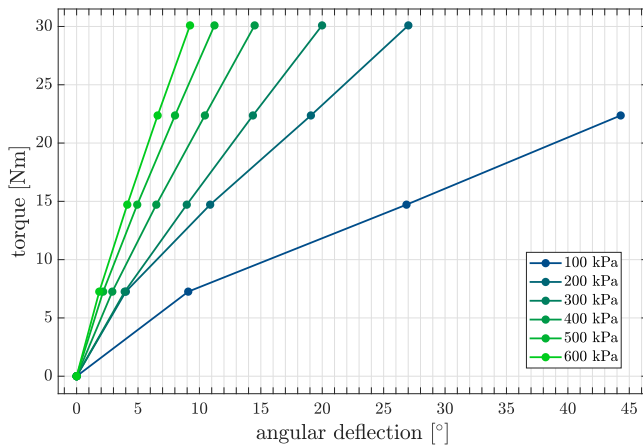


Fig. 10. Adjustable stiffness is shown, as the steepness of the graphs increases for increasing pressure. The graph for one bar only includes three measurements, as the torque of 30.1 Nm could not be counteracted by the FHA.

with the rotary drive. In Fig. 11, we present a measurement of the bit-wise change in position over the bit-wise change in the pressure signal that the PLC is commanding. The used 17-bit encoder delivers a resolution of 0.0027° per bit. We use the two FHAs 1 and 3, which are on opposite sides of the drive shaft, to show that we can avoid the stick-slip phenomenon. Both FHAs are inflated with 50 kPa and then the pressure in FHA 3 is increased by 1 bit every 10 ms. This results in the smooth movement depicted in Fig. 11.

In order to use the rotary drive in real-world applications, it is necessary that a given position can be attained. We use a simple PI-control to show that it is possible to control the drive unit and limit the effects such as overshoot or steady state offset after ten seconds. The resulting pressurization is achieved in combination with a mapping which splits the directed torque of the PI-controller onto the different FHAs,

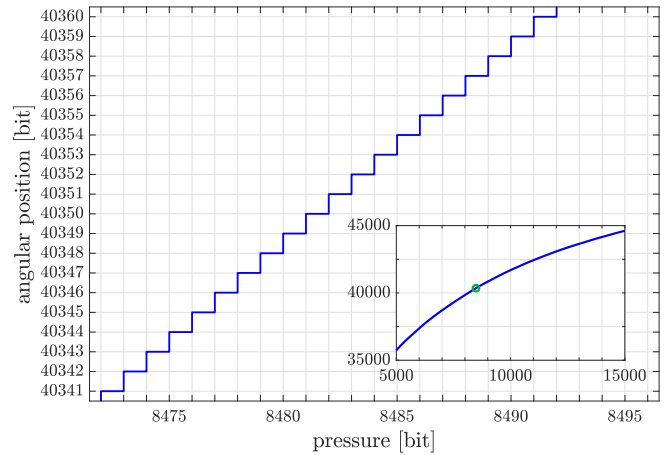


Fig. 11. Change of the position value in bit over change of the pressure value in bit, area with ideal characteristics.

similar to the mappings presented in [22]. In Fig. 12, the step-response to the position input of 135° , with starting position at 0° , is depicted. The graph corresponding to the input is labeled 'step input'. To define the movement of the rotary drive, we generate a trajectory, labeled 'trajectory', between starting and set-point position, which is furthermore the input for the controller. The resulting step-response is labeled 'position'. The overshoot for the positioning is less than 0.5% and precise positioning is achieved within 60 seconds. Thus, the rotary drive can be controlled with the available mechatronic control system and precise positioning is possible.

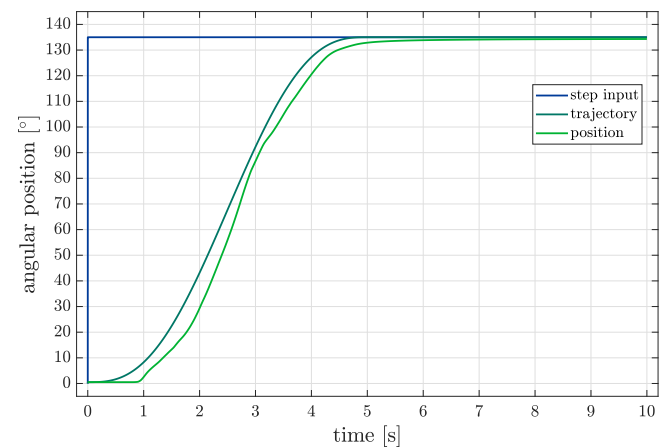


Fig. 12. Step response to a step input of 135° .

V. CONCLUSIONS AND FUTURE WORK

We present, explain, model and characterize the new pneumatic FHAs. The actuators exert a maximum force of 8089 N onto a roller element at an active length of 200 mm and a pressure of 600 kPa. Moreover, we present a rotary drive design that comprises four FHAs. We model the static torque distribution, based on the approximated measurements of the FHAs, and we compare the calculated data to measurement data of the realized laboratory test stand. The

maximum continuous torque possible is 63.11 Nm and 360° continuous rotation is possible. The rotary drive features intrinsic compliance and we present measurements of the adjustable stiffness. Furthermore, the stick-slip phenomenon cannot be observed, and, as a result, precise positioning is possible with the rotary drive. As proof, we show that the system is in ideal areas able to reach every bit of the 17-bit encoder.

In the current work, we presented the FHAs for the first time and we only investigated one specific type of FHA. Hence, in future work all design parameters and their effects on the resulting characteristics could be investigated in a parameter study. Regarding the FHA, live cycle tests would be of great interest to evaluate the durability of the FHAs. This knowledge is very helpful for the suitable design of FHAs, drive units and the later use of these systems in potential applications. In future work, the presented basic force model of the FHA can be improved. A more accurate model could precisely account for the deformation of the fire hose due to the roller.

Furthermore, in the presented drive design, the FHAs show a squeeze-out effect that could be reduced or avoided completely with an improved design of the rotary drive. Moreover, the use of bigger valves could be investigated in future research since we expect this to be the basic step to realize quicker responses to control inputs. Additionally, in further research more advanced control approaches could be investigated.

Finally, a multitude of suitable applications could be realized and evaluated.

APPENDIX

TABLE I

MECHANICAL DESIGN PARAMETERS OF THE INVESTIGATED FHAs AND OF THE REALIZED ROTARY DRIVE

Parameter and Description	Value	Unit
l_{fha} , active length of the FHA	200	mm
n , number of FHAs used	4	quantity
r_1 , eccentricity of the roller element	20	mm
r_2 , radius of the roller element	42,5	mm
$P7_x$, x-position of Point P7	0	mm
$P7_y$, y-position of Point P7	-80.5	mm
type of fire hose used for FHA	C52	type
nominal inner diameter of FHA	52	mm
length of the lids	34	mm
total length of the fire hose used for the FHA	313	mm

REFERENCES

[1] A. Albu-Schäffer, S. Haddadin, C. Ott, A. Stemmer, T. Wimböck, and G. Hirzinger, "The DLR lightweight robot: design and control concepts for robots in human environments," *Industrial Robot: an international journal*, vol. 34, no. 5, pp. 376–385, Aug. 2007.

[2] S. Rader, L. Kaul, P. Weiner, and T. Asfour, "Highly integrated sensor-actuator-controller units for modular robot design," in *2017 IEEE International Conference on Advanced Intelligent Mechatronics (AIM)*. IEEE, July 2017, pp. 1160–1166.

[3] T. Hoshi and H. Shinoda, "Robot skin based on touch-area-sensitive tactile element," in *Proceedings 2006 IEEE International Conference on Robotics and Automation, 2006. ICRA 2006.*, May 2006, pp. 3463–3468.

[4] Y. Ohmura, Y. Kuniyoshi, and A. Nagakubo, "Conformable and scalable tactile sensor skin for curved surfaces," in *Proceedings 2006 IEEE International Conference on Robotics and Automation, 2006. ICRA 2006.*, May 2006, pp. 1348–1353.

[5] G. Cannata, M. Maggiali, G. Metta, and G. Sandini, "An embedded artificial skin for humanoid robots," in *2008 IEEE International Conference on Multisensor Fusion and Integration for Intelligent Systems*, Aug. 2008, pp. 434–438.

[6] V. Duchaine, N. Lauzier, M. Baril, M. Lacasse, and C. Gosselin, "A flexible robot skin for safe physical human robot interaction," in *2009 IEEE International Conference on Robotics and Automation*, May 2009, pp. 3676–3681.

[7] J. P. Whitney, M. F. Glisson, E. L. Brockmeyer, and J. K. Hodgins, "A low-friction passive fluid transmission and fluid-tendon soft actuator," in *2014 IEEE/RSJ International Conference on Intelligent Robots and Systems*, Sept. 2014, pp. 2801–2808.

[8] J. T. Stoll and A. Pott, "A compliant, high precision, pneumatic rotary drive for robotics," in *International Symposium on Robotics*. VDE VERLAG GMBH, Berlin, Offenbach, June 2018, pp. 1–7.

[9] J. T. Stoll, K. Schanz, and A. Pott, "A compliant and precise pneumatic rotary drive using pneumatic artificial muscles in a swash plate design," in *2019 IEEE International Conference on Robotics and Automation (ICRA)*, May 2019, pp. 3088–3094.

[10] O. Ivlev, "Modular multi-sensory fluidic actuator with pleated rotary elastic chambers," in *IFAC Proceedings*, vol. 39, no. 16, Sept. 2006, pp. 271–276.

[11] S. D. Prior, P.R. Warner, A.S. White, J.T. Parsons, and R. Gill, "Actuators for rehabilitation robots," *Mechatronics*, vol. 3, no. 3, pp. 285–294, June 1993.

[12] S. D. Prior and A. S. White, "Measurements and simulation of a pneumatic muscle actuator for a rehabilitation robot," *Simulation Practice and Theory*, vol. 3, no. 2, pp. 81–117, 1995.

[13] O. Ivlev, "Soft fluidic actuators of rotary type for safe physical human-machine interaction," in *2009 IEEE International Conference on Rehabilitation Robotics*, June 2009, pp. 1–5.

[14] D. Baiden and O. Ivlev, "Independent torque and stiffness adjustment of a pneumatic direct rotary soft-actuator for adaptable human-robot-interaction," in *2014 23rd International Conference on Robotics in Alpe-Adria-Danube Region (RAAD)*, Sept. 2014, pp. 1–6.

[15] A. Wilkening, S. Hacker, H. Stppler, L. Drselén, and O. Ivlev, "Experimental and simulation-based investigation of polycentric motion of an inherent compliant pneumatic bending actuator with skewed rotary elastic chambers," *Robotics*, vol. 6, no. 1, 2017.

[16] B. Kägi, "Antriebsvorrichtung zur Ausführung einer Schwenk- oder Drehbewegung durch flüssiges oder gasförmiges Druckmedium," German Patent DE 2 351 990 A1, 1973.

[17] O. Juichi, "Motor for generating rotary motion using pressure medium," Japanese Patent JPS 3 105 280 A, 1988.

[18] C. Erker, "Gerät zur Nutzung der Druckdifferenz von Gas oder Flüssigmedien durch deren Wandlung in Rotationsbewegung," German Patent DE 102 008 049 293 A1, 2008.

[19] J. Stoll, "Drehantrieb," German Patent DE 102 016 217 198 A1, Sept. 09, 2018.

[20] C. Canudas de Wit, H. Olsson, K. J. Astrom, and P. Lischinsky, "A new model for control of systems with friction," *IEEE Transactions on Automatic Control*, vol. 40, no. 3, pp. 419–425, Mar. 1995.

[21] B. N. Persson, O. A. and F. Mancosu, V. Peveri, V. Samoilov, and I. M. Sivebæk, "On the nature of the static friction, kinetic friction and creep," *Wear*, vol. 254, no. 9, pp. 835–851, 2003.

[22] J. T. Stoll, K. Schanz, and A. Pott, "Mechatronic control system for a compliant and precise pneumatic rotary drive unit," *Actuators*, vol. 9, no. 1, Dec. 2019.